



Contents lists available at ScienceDirect

## International Journal of Plasticity

journal homepage: [www.elsevier.com/locate/ijplas](http://www.elsevier.com/locate/ijplas)

# Molecular dynamics modeling of NiTi superelasticity in presence of nanoprecipitates



Piyas Chowdhury<sup>a</sup>, Luca Patriarca<sup>a</sup>, Guowu Ren<sup>b</sup>, Huseyin Sehitoglu<sup>a,\*</sup>

<sup>a</sup> Department of Mechanical Science and Engineering, University of Illinois at Urbana-Champaign, 1206 W. Green St., Urbana, IL, 61801, USA

<sup>b</sup> Institute of Fluid Physics, Chinese Academy of Engineering Physics, Mianyang, 621999, China

## ARTICLE INFO

### Article history:

Received 13 November 2015

Received in revised form 28 December 2015

Available online 2 February 2016

### Keywords:

A. Phase transformation

A. Microstructures

A. Twinning

B. Constitutive behaviour

Shape memory alloys

## ABSTRACT

The presence of nano-sized coherent precipitates is well known to have crucial impact on the mechanical behaviors of a broad class of superelastic alloys. As a representative material, the pseudoelasticity of austenitic NiTi alloy in presence of a lenticular coherent Ni<sub>4</sub>Ti<sub>3</sub> precipitate is investigated using atomic scale simulations. We predict the local stress gradient at the matrix-precipitate interface induced by inter-lattice atomic disregistry. The calculated stress distribution conforms to the latest high resolution electron microscopy measurements in the literature. Due to the presence of the local disturbance fields, the preference for activating different martensitic variants, given the uni-directionality thereof, is influenced substantially. The resultant constitutive attributes are thus observed to undergo adjustments in terms of reduced transformation stress, strain and hysteresis in general agreement with experimental literature.

© 2016 Elsevier Ltd. All rights reserved.

## 1. Introduction

Since their discovery in the early 1950s (Buehler et al., 1963; Chang and Read, 1951), the superelastic shape memory alloys (SMA) have emerged as one of the most widely used multi-functional materials. In today's technology-driven world, the usage spectrum for these materials has widened extensively to span bio-medical, aerospace and automotive industries (Schetky, 1979; Yamauchi et al., 2011). To meet the specific requirements of modern applications, there exists an ever-mounting need for advancing new alloys with superior superelastic potential. To that end, strategies to fine-tune the microstructural features are being pursued rigorously both on experimental and theoretical grounds. Among the ongoing quests, the introduction of nanometer sized coherent precipitates, via optimizing thermo-mechanical treatments, currently stands as the singular most prospective as well as practical tactic (Ma et al., 2013; Miyazaki et al., 1984). Microstructurally, a stress-induced reversible transformation between two ordered phases triggers the observed strain recovery under isothermal conditions (Otsuka and Ren, 2005; Sehitoglu et al., 2001). The presence of nanoscale precipitates is known to drastically affect the transformation hysteresis, the orientation dependence and magnitude of transformation stress as outlined by Sehitoglu and others (Chumlyakov et al., 1997; Johnson et al., 2005; Khalil-Allafi et al., 2002; Sehitoglu et al., 2000). So influential is the effect of coherent precipitation that there exist newly proposed alloys, despite not being ordered crystals, demonstrating enhanced recoverability due solely to the prevalence of precipitates (Chumlyakov et al., 2014; Sehitoglu et al., 2002; Tanaka

\* Corresponding author. Tel.: +1 217 333 4112; fax: +1 217 244 6534.

E-mail address: [huseyin@illinois.edu](mailto:huseyin@illinois.edu) (H. Sehitoglu).

et al., 2010). The principal role of these coherent precipitates is to create microscopic stress gradients as a direct consequence of the inter-lattice mismatch, which in turn sets a preference for uni-directional transformation variants. Evidently, for the current generation of scientists and researchers, an atomic level understanding of the precipitate-matrix interplay can prove instrumental in forwarding new alloys and service components. However, the present limitations of even most modern experimental techniques preclude *in-situ* investigation of the physical micromechanisms therein with the atomic-scale resolution. Thus, one can immediately notice the critical need for an atomistic theoretical framework, free of adjusting parameters, to examine the mechanistic foundation for the general constitutive behaviors of precipitated superelastic alloys. The present paper addresses these very concerns with molecular dynamics modeling, particularly utilizing a novel improved pair-potential. Fig. 1 puts the current study into perspective.

For our objective, we select near equiatomic NiTi alloys as the candidate material for study. The NiTi alloys are one of the most important classes of shape memory alloys (exhibiting pronounced superelasticity above austenite finish temperature,  $A_f$ ) both from research and application perspectives. These alloys are studied extensively via experiments, and long known to demonstrate well-defined  $\text{Ni}_4\text{Ti}_3$  precipitation upon suitable thermo-mechanical treatments (Fig. 2). Early x-ray diffraction studies affirmed that the lattice structure of the  $\text{Ni}_4\text{Ti}_3$  precipitate is of rhombohedral type (Saburi et al., 1986; Tadaki et al., 1986). A coherent boundary is characterized by a high degree of atom-by-atom correspondence between the two adjoining lattices (i.e. the cubic matrix and the rhombohedral precipitate). The coherency of a precipitate is a strong function of its size and shape. Through electron microscopy, the  $\text{Ni}_4\text{Ti}_3$  precipitates are typically found to be of oblate spheroid geometry, lying on the  $\{111\}_{B2}$  family of planes. Fig. 2 shows the most commonly observed microstructure morphology with the presence of  $\text{Ni}_4\text{Ti}_3$  precipitates. Precipitates with relatively small disc-diameters (typically of 5–10 nm) maintain coherent boundaries with the matrix material (Treppmann et al., 1995). Thus, with a substantial inter-lattice registry at the shared periphery, the small coherent precipitates induce elastic disturbance fields along the boundary. The origin of these fields can be attributed to the very discreteness of the neighboring crystals, which consist of atoms as building blocks at the sub-crystal level. The non-continuum nature of the atomistically mismatching lattices (i.e. the austenitic B2 matrix and the rhombohedral  $\text{Ni}_4\text{Ti}_3$ ) (Gall et al., 1999; Tirry and Schryvers, 2005) gives rise to elastically stretched atoms at the boundary. By contrast, semi-coherent to incoherent precipitates (i.e. with diameter  $\gg 10$  nm), are characterized by the presence of a gradually increasing number of interfacial dislocations, which serve to mitigate the interfacial disturbances. Essentially, the sub-nanometer sized precipitates are more influential in terms of generating internal stress/strain fields in the NiTi alloy microstructure. Consequently, the coherent precipitates strongly influence the material preference for the nucleation and the growth of the uni-directional martensitic variants (Bataillard et al., 1998) at the micro level. The resultant deformation characteristics are macroscopically manifested in terms of decreased transformation stress, strain, and hysteresis as reported in the experimental literature. Most recently, using high resolution electron microscopy (Schryvers et al., 2006; Tirry and Schryvers, 2005), have measured the strain gradient near a  $\text{Ni}_4\text{Ti}_3$  particle in an austenitic matrix, which quite interestingly demonstrates a non-uniform profile. From theoretical standpoint, validity of any model can be checked against such findings. To develop a full understanding of the chain of micromechanisms contributing to the macroscale behaviors, one ought to delve deeper into the atomic level phenomena as outlined heretofore.

A number of theoretical approaches have been undertaken in the earlier literature to understand NiTi constitutive behaviors (Bouvet et al., 2004; Sedláč et al., 2012; Zaki and Mounni, 2007). Most of these models based on the principles of thermodynamics, finite element and self-consistent methods address the continuum aspects of the problem (Bhattacharya, 2003; Boyd and Lagoudas, 1996; Patoor et al., 1996; Shaw, 2000; Song et al., 2013; Yang and Li, in press). Most noteworthy approach to address the precipitate problem is the Eshelby-type analysis (Mura, 2012) capturing the internal/external stress/strain distributions for various precipitate geometries. Sehitoglu et al. explained the biased variants due to the precipitate fields with micro-mechanical calculations (Gall et al., 1999). However, as pointed out earlier, the fundamental effects of a

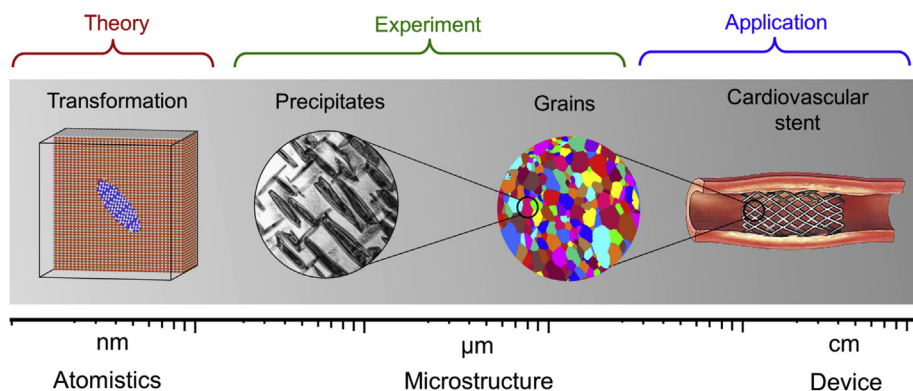


Fig. 1. Figure – The present research in perspective (the EBSD and the TEM images are from Wang et al. (2015) and Gall et al. (1999) respectively; the stent is from: <http://www.britannica.com/science/aneurysm>).

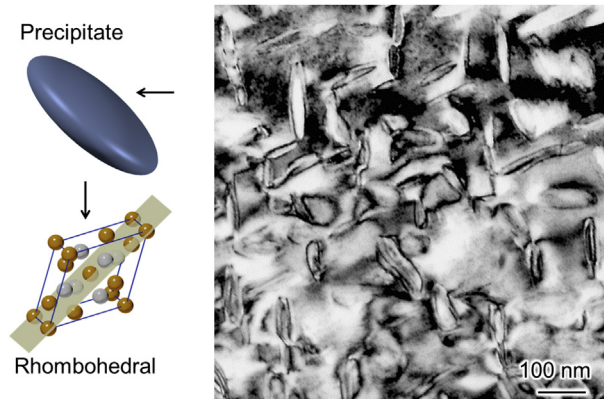


Fig. 2. Transmission electron microscopy (TEM) image of  $\text{Ni}_4\text{Ti}_3$  precipitates in an austenitic matrix [12].

precipitate disturbance fields originate from the atomistic interactions (Khalil-Allafi et al., 2002) at the discrete lattice level. To that end, with the advent of superior computer power, the last decade has witnessed a surge in the atomic-scale modeling. Most recently, quantum mechanics based treatments have been forwarded, predicting the elastic anisotropy of the  $\text{Ni}_4\text{Ti}_3$  lattice founded on the sub-lattice electronic structure (Wagner and Windl, 2009). However, the *ab initio* endeavors are currently limited to small systems due to a requirement of very high computing capacity (Chowdhury et al., 2015b), and hence unable to capture the mesoscopic deformation scenarios. However, one can resort to mesoscale molecular dynamics (MD) simulations to address much larger crystals consisting of millions of atoms, utilizing pair potential based bonding descriptions.

As of today, most MD simulations on the strain-recovering alloys are confined to NiTi crystals in solutionized conditions (i.e. without precipitates) (Cisse et al., 2016; Farkas et al., 1996; Lai and Liu, 2000; Mutter and Nielaba, 2010; Zhong et al., 2012). The primary objective has remained as capturing a broad spectrum of NiTi behaviors. To compare predictions with experimental findings, the principal attributes to be modeled are threefold: (a) the size/shape of stress–strain hysteresis, (b) the martensitic phase transformation (i.e.  $B2 \leftrightarrow B19'$ ) at the crystal level, and (c) the stability of individual phases under various thermo-mechanical situations. To that end, the existing literature reports several accomplishments. For example, Farkas et al. (1996) proposed a pair potential and addressed the B2 lattice cohesive energy. Lai and Liu predicted the melting behavior thereof based on another potential. Most recently, Zhu and co-workers (Mirzaeifar et al., 2014; Zhong et al., 2012) adapted Lai and Liu's potential to study martensitic phase transformation both in nanowire and bulk crystal configurations. Similarly, Mutter and Nielaba (2011, 2013) added modifications to Lai's original potential to predict temperature/composition dependent transformation behaviors. While the literature models succeeded in theorizing solutionized crystal behaviors, there still exists a need for studying how the aforementioned attributes are modified by nanoprecipitates. It is important to note that the crystallographic interaction between the matrix (cubic B2 or monoclinic B19') and precipitate (rhombohedral) is rather complex and entails a rather stringent accuracy from the pair-potential. Particularly, it is imperative that the potential be capable of predicting elastic moduli accurately of individual crystal structures. In this work, we use a newly developed Finnis-Sinclair type potential (descriptions provided in next section) to achieve such a feat. We employ several improvement tactics such as fine-tuning the cut-off behavior as well as accurately fitting the cross-interaction energy terms using density functional theory parameters. We particularly aim to investigate the *in-situ* atomic-scale mechanism of how a coherent  $\text{Ni}_4\text{Ti}_3$  particle influences: (a) the martensitic phase transformation and (b) the associated stress–strain response.

The current work, based on the NiTi austenite precipitated with lens-shaped  $\text{Ni}_4\text{Ti}_3$ , can be deemed as a necessary and timely contribution. This analysis serves to represent the generic effects of a nanoprecipitate on the superelasticity, and essentially pave the way for extending current modeling approach to address similar class of materials.

## 2. Methods

### 2.1. Pair potential

Central to the concept of pair potential is the notion that the positively charged atomic nuclei interconnect with each other via homogeneously distributed electron clouds (Fig. 3). This very special electronic bonding landscape can be mathematically re-constructed by considering (i) the pair-wise potential energy,  $\phi_{ij} = \phi_{ij}(r_{ij})$  representing the close-range repulsive and long-range attractive forces (between atoms  $i$  and  $j$  separated by  $r_{ij}$ ), and (ii) the embedding energy functional,  $F_i$  which implies energy required to embed atoms into an electronic cloud (as contributed by all other atoms of the system). The total electron density, at the site of a certain atom,  $i$ , is approximated by a simple linear superposition of electron cloud contributions of all neighboring atoms,  $j$  i.e.  $\rho_{ij} = \rho_{ij}(r_{ij})$ . Thus, the total potential energy surface can be represented by the Eq. (1):

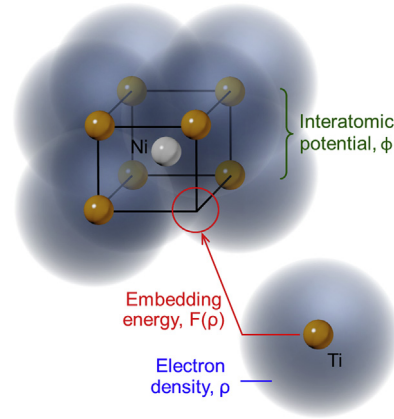


**Fig. 3.** The concept of pair-potential in MD simulations. The metallic bonding is reproduced by considering the functions,  $\rho$ ,  $\phi$  and  $F$ .

$$E_{\text{total}} = \sum_{i \neq j} \phi_{ij} + \sum_{i \neq j} F_i \left( \sum_{j \neq i} \rho_{ij} \right) \quad (1)$$

For NiTi binary alloy system, one can narrow down to the following functions:  $F_{\text{Ni}}$ ,  $F_{\text{Ti}}$ ,  $\rho_{\text{Ni-Ni}}$ ,  $\rho_{\text{Ti-Ti}}$ ,  $\rho_{\text{Ni-Ti}}$ ,  $\phi_{\text{Ni-Ni}}$ ,  $\phi_{\text{Ti-Ti}}$  and  $\phi_{\text{Ni-Ti}}$ . Mishin and co-workers (Mishin, 2004; Zope and Mishin, 2003) extensively discussed the terms for pure Ni and Ti. We model the inter-species  $\rho_{\text{Ni-Ti}}$  and  $\phi_{\text{Ni-Ti}}$  to capture the full spectrum of the potential surface of Ni–Ti system. The development strategy consists of: (a) conducting density functional theory (DFT) simulations using the *Quantum Espresso* (Giannozzi et al., 2009) to obtain parameters of importance, to be fitted, and (b) formulation a cubic spline functional form for both  $\rho_{\text{Ni-Ti}}$  and  $\phi_{\text{Ni-Ti}}$  (as function of  $r_{ij}$ ). The *Quantum Espresso* is an open-source code for modeling materials electronic structure based on DFT formalisms. Further details for interested readers are provided at: <http://www.quantum-espresso.org>. The DFT-extracted energy versus volume data plus experimentally determined (from literature) cohesive energies will then be used to determine the cubic spline constants.

We use a cubic fitting expression of the form:

$$\rho(r) \text{ or } \phi(r) = \sum_{\alpha} a_{\alpha} (r_{\alpha} - r)^3 H(r_{\alpha} - r) \quad (2)$$

where  $\alpha$  denotes a particular knot of the curve; the Heaviside function,  $H(r - r_{\alpha}) = 1$  for  $(r - r_{\alpha}) \geq 0$  and  $H(r - r_{\alpha}) = 0$  for  $(r - r_{\alpha}) < 0$ . The coefficients  $a_{\alpha}$  are determined at known  $r_{\alpha}$  values up to the cut-off radius (0.52 nm) by optimization method. To that end, we assume an objective function ( $Z$ ) of the following form, to be minimized, considering the fitting weight ( $w_{\beta}$ ):

$$Z = \sum_{\beta} w_{\beta} (Y(r, a_{\beta}) - Y_{\beta 0}) \quad (3)$$

where  $Y_{\beta 0}$  is the target value of the parameter to be fitted (e.g. elastic constant, energy from experiments and/or DFT predictions) and  $Y(r, a_{\beta})$  is fitting value to be adjusted with an adjustable  $a_{\beta}$ . Setting a value for  $w_{\beta}$  manually,  $a_{\beta}$  values are determined corresponding to the a minimized  $Z$ , and then inserted in Eq. (2). It should be noted that different values of  $w_{\beta}$  only mean different number of iterations (to minimize the function,  $Z$ ) to ultimately converge on the final target value. Thus, the cross-species functions  $\rho_{\text{Ni-Ti}}$  and  $\phi_{\text{Ni-Ti}}$  are numerically produced. Specifically, the target variables to be fitted comprise: (a) the energy versus volume relations for B2, B19, B19', BCO (body-centered orthogonal) crystals and imaginary B1-NiTi, L1<sub>2</sub>-Ni<sub>3</sub>Ti and L1<sub>2</sub>-NiTi<sub>3</sub> compounds (from *Quantum Espresso* based calculations), (b) experimentally determined B2 elastic constants ( $C_{11}$ ,  $C_{12}$  and  $C_{44}$ ) from earlier literature (Mercier et al., 1980), and (c) the cohesive energies for pure species (Mishin, 2004; Zope and Mishin, 2003).

Following the foregoing methodology, the entire potential energy surface is constructed as given in Eq. (1). Due to the accuracy of the fitting process, the current potential provides a considerably better prediction of elastic constants (Tables 1 and 2). As a result, we are able to conduct accurate molecular dynamics (MD) simulations of the phase transformation as well as the effects of lattice mismatch (between the B2 matrix and rhombohedral precipitate lattice). The most salient feature of the current potential is the accurate prediction of the stress levels during deformation (as is presented subsequently). The predicted flow stress levels were predicted in MPa levels (where typical MD simulation based stresses are in GPa range). Another important consideration for accurate MD modeling is the precise atomic positions (of both B2 and B19' lattices). Positioning of the atoms would essentially dictate the NiTi constitutive behaviors subjected to different crystal orientations

and loading senses (i.e. tension, compression). For example, the fractional positions for basis atoms in monoclinic B19' lattice are experimentally (Kudoh et al., 1985) reported to be: Ti  $\equiv$  (0, 0, 0) and (0.5672, 0.5, 0.1648) and Ni  $\equiv$  (0.4588, 0, 0.6196) and (0.1084, 0.5, 0.5452). The literature potential (Zhong et al., 2012) notes the positions as follows: Ti  $\equiv$  (0, 0, 0) and (0.5, 0.5, 0) and Ni  $\equiv$  (0.5, 0, 0.5) and (0, 0.5, 0.5). In comparison, the current predictions (upon energetically minimizing the crystal) are: Ti  $\equiv$  (0, 0, 0) and (0.6973, 0.5, 0.3413) and Ni  $\equiv$  (0.4906, 0, 0.6645) and (0.2067, 0.5, 0.6769) in better agreement with the experimentally reported ones. The fact that the predicted constitutive responses and the associated phase transformations are in good agreement with literature is attributed to the foregoing improvements in the potential (most importantly, the correct elastic moduli and atomic positions).

## 2.2. MD simulation procedure

The open source software LAMMPS (Plimpton, 1995) (*Large-scale Atomic/Molecular Massively Parallel Simulator*) developed at Sandia National Laboratories, USA (<http://lammps.sandia.gov>) was used to conduct MD simulations. The atomic configuration viewer Ovito (Stukowski, 2010) (<http://ovito.org>) was utilized to analyze the evolution of crystal structures.

First, we created the austenitic NiTi single crystals of B2 type unit cells (with  $a_{B2} = 3.021\text{\AA}$ ) using the basis: Ni  $\equiv$  (0 0 0) and Ti  $\equiv$  (0.5 0.5 0.5). Then, separately a lens-shaped Ni<sub>4</sub>Ti<sub>3</sub> precipitate is constructed, to be embedded in a B2 austenite matrix as shown in Fig. 4(a). The primitive unit cell of Ni<sub>4</sub>Ti<sub>3</sub> precipitate is of rhombohedral type. The atomic positions for the basis atoms for this unit cell are taken from the X-ray diffraction literature (Saburi et al., 1986; Tadaki et al., 1986). The lattice variables for the rhombohedral unit cell are:  $a_R = 6.704\text{\AA}$  and  $\alpha_R = 113.85^\circ$ . As presented in Fig. 4(b), the oblate-spheroid precipitate is constructed with major and minor axis being 70Å and 24Å respectively. It consists of 2681 Ni atoms and 2017 Ti atoms. The minor axis of the precipitate is parallel to the [111]<sub>R</sub> crystal direction. The host matrix consists of B2 unit cells with lattice constant,  $a_{B2} = 3.021\text{\AA}$ . The oblate ellipsoid is inserted into the austenitic NiTi B2 matrix with the [111]<sub>R</sub> plane parallel to the [111]<sub>B2</sub> plane (Fig. 5), and energetically minimized in molecular statics simulations.

The energy minimization is conducted using the conjugate gradient energy algorithm. The size of the cubic crystal (with each side being 30 nm) is selected based on the convergence of physical observables (e.g. temperature, pressure, kinetic and potential energy) to the system size independence. It should be noted that the convergence is established upon a multitude of simulations for various sizes of the simulation representative volumes. The crystals represent bulk material (i.e. without any

**Table 1**

Elastic constants (in GPa) of B19' from the current potential, a literature potential by Zhong et al. (2012), and DFT calculations (Wang and Sehitoglu, 2014).

Elastic constants (GPa)	B19'		
	Current potential	Literature DFT (Wang and Sehitoglu, 2014)	Literature potential (Zhong et al., 2012)
C <sub>11</sub>	206	209	692
C <sub>12</sub>	72	114	400
C <sub>13</sub>	103	102	326
C <sub>15</sub>	2	1	292
C <sub>22</sub>	252	234	1135
C <sub>23</sub>	120	139	222
C <sub>25</sub>	-7	-7	125
C <sub>33</sub>	218	238	303
C <sub>35</sub>	-16	27	175
C <sub>44</sub>	37	77	286
C <sub>46</sub>	-2	-5	110
C <sub>55</sub>	41	23	215
C <sub>66</sub>	43	72	114
Bulk modulus, B	141	154	447
Shear, modulus, $\mu$	50	56	202
Young's modulus, E	133	150	526
Poisson's ratio, $\nu$	0.34	0.34	0.3

**Table 2**

Elastic constants (in GPa) for B2 crystal from current potential, a literature potential by Zhong et al. (2012), and experimental measurements by Mercier et al. (1980).

Elastic constants (GPa)	B2		
	Current potential	Literature experiment (Mercier et al., 1980)	Literature potential (Zhong et al., 2012)
C <sub>11</sub>	146	162	205
C <sub>12</sub>	122	129	136
C <sub>44</sub>	35	35	47
Bulk modulus, B	130	140	159
Shear, modulus, $\mu$	26	28	42
Young's modulus, E	73	78	116
Poisson's ratio, $\nu$	0.41	0.41	0.38

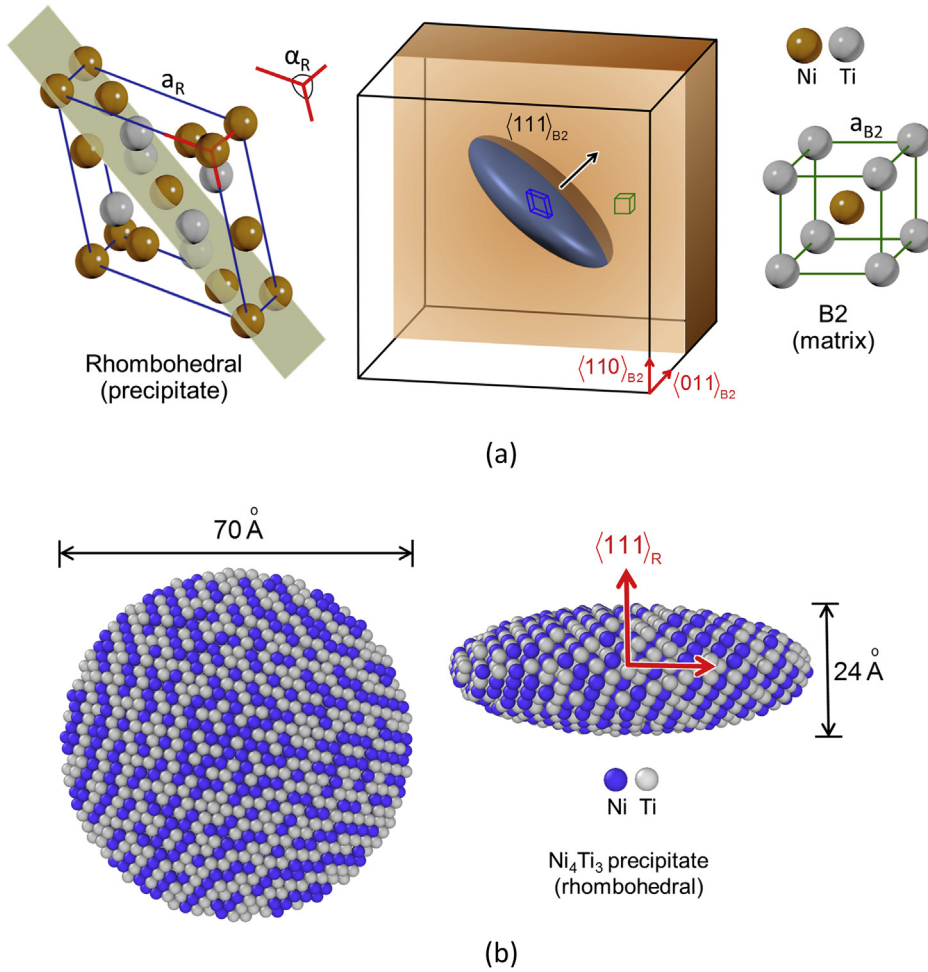


**Fig. 4.** (a) – A  $\text{Ni}_4\text{Ti}_3$  precipitate of rhombohedral primitive unit cell embedded in a B2 austenitic matrix. The precipitate lies on the  $\langle 111 \rangle_{B2}$  plane. (b) – The atomistic configuration of the lens-shaped  $\text{Ni}_4\text{Ti}_3$  precipitate. The oblate spheroid is constructed with the  $\langle 111 \rangle_R$  plane parallel to  $\langle 111 \rangle_{B2}$ . (For interpretation of the references to colour in this figure legend, the reader is referred to the web version of this article.)

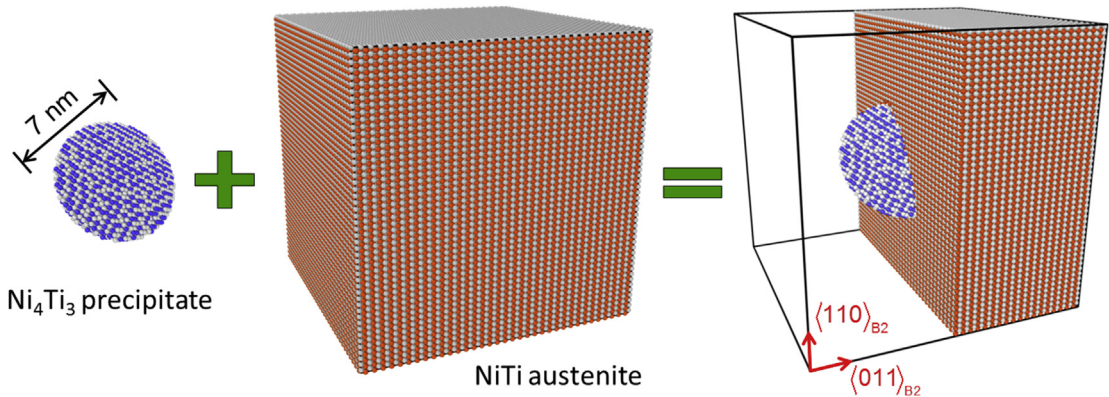


**Fig. 5.** The creation of the matrix-precipitate composite. The pre-constructed rhombohedral precipitate of lens shape is inserted into a B2 lattice and energetically relaxed in molecular statics simulations.

free surface or dangling bonds) as ascertained by enforcing periodic boundary condition on the crystal facets (Chowdhury et al., 2014a, 2013). The number of atoms in a typical simulation supercell was about  $1 \times 10^6$ , which is sufficiently large to avoid any size- and/or periodicity-induced artifacts (Frenkel and Smit, 2001). An  $nph$  ( $n \rightarrow$  number of atoms,  $p \rightarrow$  pressure and  $h \rightarrow$  enthalpy) ensemble was employed for non-equilibrium deformation simulations with a constant number of atoms and zero external pressure. A steady temperature is established prior to each non-equilibrium simulation via a thermostating algorithm coupled with energy minimization scheme. A Velocity Verlet time-integration scheme was used to conduct the time-step advancement during the deformation simulations (Chowdhury, 2011). The stress–strain responses reported in this letter are computed based on the concept of virial stress (which is the atomistically equivalent quantity of the conventional Cauchy stress) (Tadmor and Miller, 2011). The virial stress is conventionally defined in its simplest form as follows:

$$\sigma^{\text{virial}} = \frac{1}{\text{volume}} \left( \text{kinetic energy} + \frac{1}{2} \sum \left( \frac{\partial \phi}{\partial \mathbf{r}} \right) \mathbf{r} \right) \quad (4)$$

### 3. Results

#### 3.1. $\text{Ni}_4\text{Ti}_3$ precipitate and elastic fields

Fig. 6(a) shows the three-dimensional distribution of the normalized stress profile scanned along the center plane of the precipitate disc. The stress data presented are averaged over a very thin-sliced plane parallel to the disc equator in order to

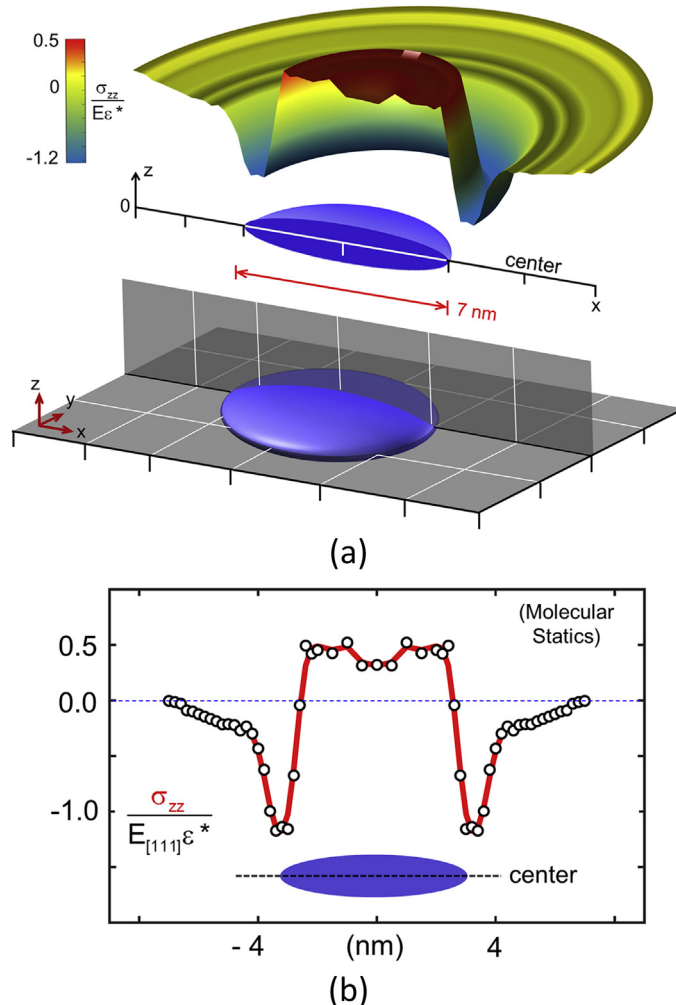


Fig. 6. (a) – The three dimensional stress profile on a plane going through the disc equator. (b) – The same data demonstrating the stress distribution along a line.

capture the correct planar stress distribution. The averaging is conducted with a spatial resolution of 2Å. Fig. 6(b) presents the  $\sigma_{zz}$  stress profile along the centerline of the precipitate as shown. The stress fields surrounding the precipitate are axisymmetric about the z axis, and mirror-symmetric about x and y axes. Therefore, the stress components  $\sigma_{yy}$  and  $\sigma_{xx}$  follow similar profiles (not shown). The stress components are normalized by the precipitate Young's modulus,  $E_{[111]} = 168$  GPa (Wagner and Windl, 2009), and the eigenstrain,  $\epsilon_{zz}^* = 0.029$  mm/mm (Li and Chen, 1997). It is observed that inside the precipitate the stress is tensile and constant, while a compressive stress peak can be discerned along the austenite–precipitate interface.

Fig. 7(a) and (b) demonstrate the computed stress distribution on a plane very close to the precipitate surface (parallel to the disc plane) as indicated. The computed near-surface stress distribution appears markedly different than the peripheral one as presented earlier in Fig. 6(a) and (b). It can be seen that near the pole (i.e. on top of the disc) the stress is constant and compressive in nature. Farther away from the pole (and also from the surface), the stress reaches a tensile maximum. On reaching the peak magnitude, the stress then gradually subsides to the bulk level (i.e. zero) with increasing distance from the interface.

The characteristic variations of the near-interface stress distribution in the matrix are in general agreement with the most recent measurements using high resolution electron microscopy by Schryvers et al. (2006) and Tirry and Schryvers (2005). Their findings suggested a very similar distribution. A maximum strain is found not at the interface itself, rather a distance away from it, which then gradually diminishes (i.e. similar to the present case). These researchers pointed out that there is a strong deviation of the measured gradient from micromechanical predictions. They attributed the apparent discrepancy to: (a) the assumption of an equal stiffness for the precipitate and the matrix in the micro-mechanical models, and (b) the deviation of the real precipitate shape from the ideal lenticular one (as presumed in the Eshelby formulations). By contrast, in the current calculations, the generated stress profile is obtained as a direct result of the atomistic misfit, circumventing both

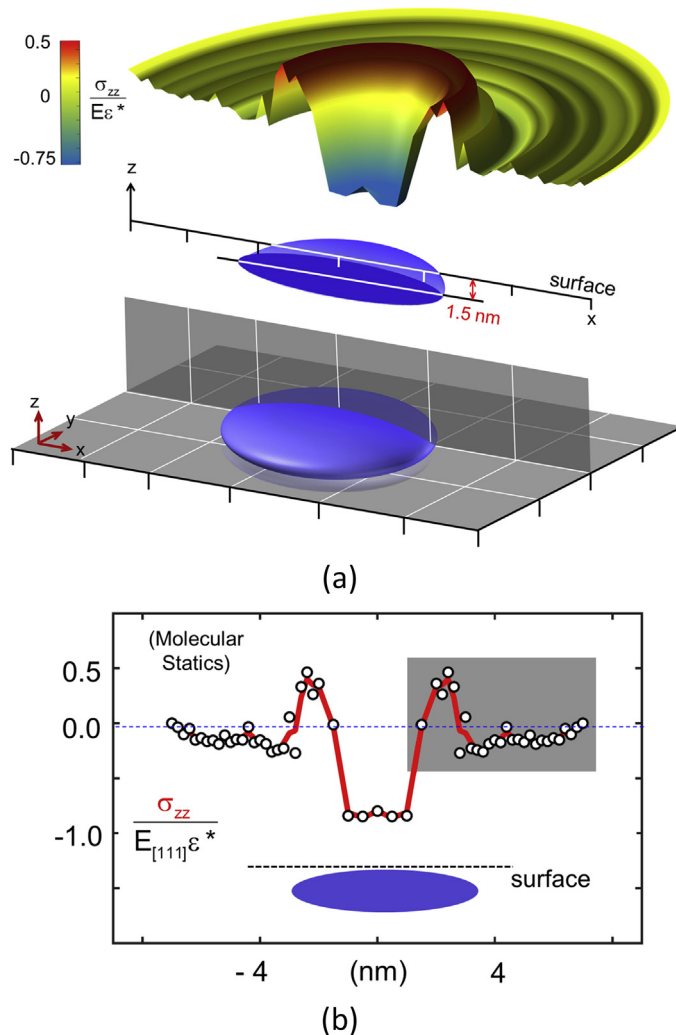
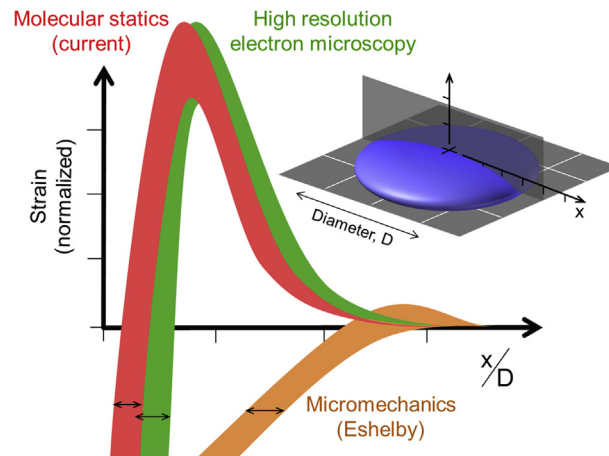


Fig. 7. (a) – The 3D stress distribution near the surface of the precipitate on a plane parallel to the disc plane. (b) – The near-surface 2D stress profile.



**Fig. 8.** A schematic comparison of the strain gradient near the precipitate surface obtained from current molecular statics simulations, high resolution electron microscopy by Schryvers et al. (2006), Tirry and Schryvers (2005) and micromechanical prediction (Gall et al., 1999). The band representation is due to the uncertainty in calculations.

constancy of stiffness and the perfect ellipsoid shape assumptions. The currently modeled interface is essentially non-continuum, and is found to deviate from the perfect ellipsoid outline upon molecular statics relaxation. The physical reason for such deviation is believed to be due to the equilibrium positions of interfacial atoms. The atoms at the periphery, following relaxation, are not aligned in a perfect elliptical outline. This physics is equivalent in principle to the formation of any material boundary, which is known to deviate from perfect geometrical shapes. Also, the moduli of the cubic matrix and the rhombohedral precipitates are not the same. In other words, the physical conditions of the precipitate in the present simulations are significantly close to that found in nature. Thus, the molecular statics based calculations provide better agreement with the experiments, unlike the micromechanical predictions. Fig. 8 provides a schematic comparison of the precipitate strain gradient near the top surface as in Fig. 6(b) (highlighted with gray shading). The comparison is conducted against the normalized distance obtained from current molecular statics simulations, high resolution electron microscopy (Schryvers et al., 2006; Tirry and Schryvers, 2005) and micromechanical predictions based on Eshelby inclusion problem (Gall et al., 1999).

Next, to understand the role of the precipitate-induced internal stresses, we conduct uniaxial compression simulations for the  $\langle 011 \rangle_{B2}$  loading orientation. In the following sections, we refer to the pristine NiTi austenitic single crystal (with no precipitate) as the “un-precipitated” and the one with the embedded  $\text{Ni}_4\text{Ti}_3$  ellipsoid as the “precipitated” crystals.

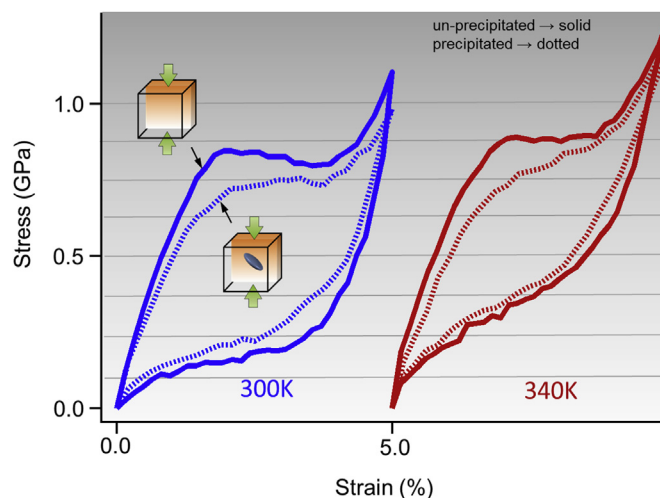


**Fig. 9.** The stress–strain responses of the precipitated and the un-precipitated austenitic crystals.

**Table 3**

Calculated values of  $\sigma_{\text{transform}}$  and  $\epsilon_{\text{transform}}$  for the precipitated and un-precipitated NiTi austenite compressed  $\langle 011 \rangle_{\text{B2}}$  in direction.

Parameter	Temperature	Un-precipitated	Precipitated
$\sigma_{\text{transform}}$ (MPa)	300 K	776	556
	340 K	787	574
$\epsilon_{\text{transform}}$	—	4.20%	3.18%
Stress hysteresis, H (MPa)	300 K	620	502
	340 K	503	370

3.2. Stress–strain behavior

The presence of the precipitate is found to reduce the transformation stress and strain under  $\langle 011 \rangle_{\text{B2}}$  compression. Fig. 9 presents the constitutive responses of the austenitic NiTi single crystals in presence/absence of the  $\text{Ni}_4\text{Ti}_3$  precipitate at 300 K and 340 K temperatures. The reported stress–strain curves are obtained for the crystals deformed to a maximum strain level of 5%. It readily follows that both the un-precipitated and the precipitated crystals demonstrate superelastic stress–strain behavior with hysteresis.

For the un-precipitated NiTi austenite at 300 K, a transformation stress,  $\sigma_{\text{transform}}$ , of 776 MPa (based on 0.2% offset method) is calculated (Chowdhury et al., 2015a). In comparison, the precipitated crystal at the same temperature experiences a reduced magnitude of  $\sigma_{\text{transform}} = 556$  MPa. At a higher temperature (340 K), the  $\sigma_{\text{transform}}$  for the un-precipitated austenite is about 787 MPa. For the precipitated crystal at 340 K, the  $\sigma_{\text{transform}}$  drops to approximately 574 MPa compared to the un-precipitated one at the same temperature.

The maximum transformation strain (i.e.  $\epsilon_{\text{transform}} = \epsilon_{\text{total}} - \epsilon_{\text{elastic}}$ ) obtained for the un-precipitated NiTi is calculated to be 4.20%. For the precipitated case, the maximum  $\epsilon_{\text{transform}}$  drops to 3.18%. These observations are consistent with early experimental literature (Gall et al., 1999; Sehitoglu et al., 2001). The calculated  $\sigma_{\text{transform}}$  and  $\epsilon_{\text{transform}}$  magnitudes of the precipitated and un-precipitated NiTi are summarized in Table 3.

The aforementioned observations can be summarized as follows.

- (a) The precipitated austenite experiences a reduction in the magnitudes of  $\sigma_{\text{transform}}$  and  $\epsilon_{\text{transform}}$  compared to those of the un-precipitated one.

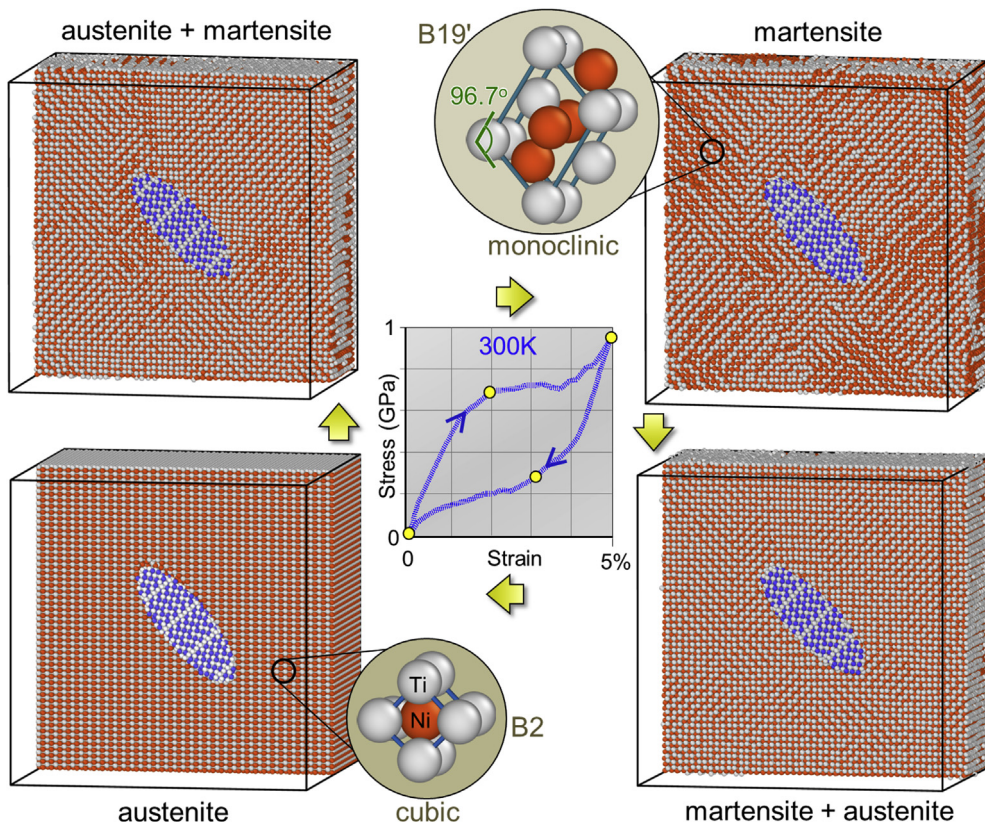


**Fig. 10.** The evolution of phase transformation during the loading/unloading the precipitated crystal.

- (b) With increasing temperature (300 K  $\rightarrow$  340 K), both the un-precipitated and the precipitated austenite experiences an increased  $\sigma_{\text{transform}}$ , and smaller hysteresis.

To unravel the mechanistic origin of the observed constitutive responses, next we analyze the atomic-scale evolution of the phase transformation processes.

### 3.3. Reversible B2 $\leftrightarrow$ B19' transformation

Fig. 10 demonstrates the atomistic snapshots of the precipitated NiTi single crystal during various stages of deformation at 300 K temperature. The crystal is sectioned in the middle to reveal the  $\text{Ni}_4\text{Ti}_3$  precipitate. We observe that the initial elastic straining (from 0% to about 1.8%) does not incur any change in the atomistic morphology of the austenitic bulk, as expected. The matrix phase remains essentially the same as the initial B2 structure, only elastically compressed along the applied loading direction. When the applied stress level reaches the critical magnitude of 556 MPa, the atoms surrounding the precipitate is observed to undergo considerable re-arrangement, indicating the initiation of B2  $\rightarrow$  B19' martensitic phase transformation. At this stage, some regions of the austenitic lattice (with B2 unit cells) start transforming into the monoclinic B19' lattice. This can be verified by a careful inspection of the lattice structure of the transformed portion of the crystal. On a closer inspection, the monoclinic non-orthogonal lattice structure can be clearly discernible. The distinctive features of the B19' unit cell are the lattice variables thereof:  $a_{\text{B19}'} = 4.0606\text{\AA}$ ,  $b_{\text{B19}'} = 4.386\text{\AA}$ ,  $c_{\text{B19}'} = 2.699\text{\AA}$  and  $\alpha_{\text{B19}'} = \gamma_{\text{B19}'} = 90^\circ < \beta_{\text{B19}'} (\approx 96.7^\circ)$ . The monoclinic unit cell structure is in stark contrast with the B2 lattice. Thus, the volumes containing the individual phases can be properly identified upon studying the unit cell structure at higher viewing (atomistic) resolutions. With continued compression (i.e. along the stress plateau), the volume fraction of the B19' martensite increases. The atoms part of the newly transformed B19' lattice also create multiple mirrored strips. This phenomenon is the direct evidence of the "internal twinning" of the B19' martensite. Such twinning process is commonly designated as the "compound" type in the literature, occurring on the  $\{001\}$  family of planes.

The internal deformation twinning process continues until the exhaustion of the austenitic material, which occurs at about 3.8% applied strain. At this point, the precipitated single crystal becomes fully martensitic (of internally twinned B19' lattice) approximately at 4% applied strain. Continuation of applied loading leads to the elastic straining of the twinned martensite, corresponding to the rising portion of stress–strain curve (from about 4% to 5%). It is worth noting that no discernible atomic re-arrangement within the  $\text{Ni}_4\text{Ti}_3$  precipitate itself is observed, as expected. The final crystal structure (at 5% applied strain) is characterized by multiple internal twins as can be seen in Fig. 10. This phenomenon is consistent with early experimental observation that the presence of precipitate curtails the detwinning process, thus facilitating the elastic straining of martensite (Trepplmann et al., 1995).

Upon unloading, the deformed crystal consisting of twinned martensite fully recovers the total strain of 5%. Mechanistically, the complete deformation recovery can be attributed to a combination of elastic relaxation and a reverse transformation, B19'  $\rightarrow$  B2. The atomistic snapshot in Fig. 10 indicates a gradually diminishing volume fraction of twinned B19' during unloading. The volume fraction of the martensitic B19' phase continuously diminishes along the lower stress plateau. The phenomenon suggests that the internally twinned B19' structure is stable only under high stress, and hence the removal of stress triggers the B19'-to-B2 transformation. Fig. 11 presents a closer atomistic view near the precipitate. Different variants of the martensite structure can be discerned. The predominance of variant 2 can be attributed to the local fields of the precipitate.

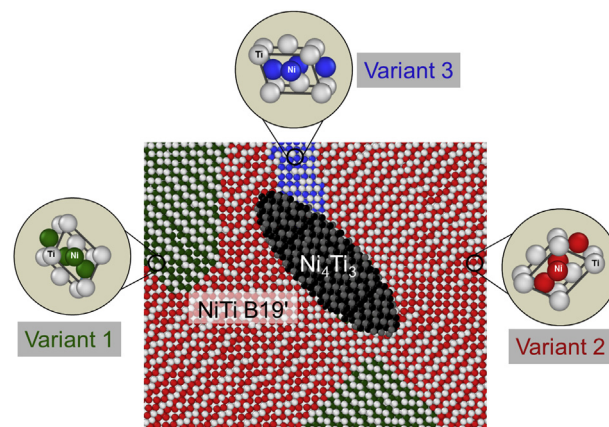


Fig. 11. Formation of different variants (of monoclinic B19' type lattice) around the ellipsoid  $\text{Ni}_4\text{Ti}_3$  precipitate (of rhombohedral lattice).

## 4. Discussion

### 4.1. Elastic fields of precipitate

The presence of  $\text{Ni}_4\text{Ti}_3$  precipitate induces substantial local stress concentration at the interface, which strongly influences the dynamics of the matrix-originated defects (e.g. propagation of twins etc.) during deformation. The origins of these stress disturbances can be twofold: (i) the initial atomic misfit at the matrix-precipitate interface (prior to any applied loads), and (ii) the inter-lattice elastic moduli mismatch, which introduces further stress concentrations during loading. Experimentally, the extent of elastic strain fields around the  $\text{Ni}_4\text{Ti}_3$  particle has most recently been quantified using high resolution electron microscopy (Tirry and Schryvers, 2005). On theoretical grounds, the problem of precipitate-matrix interaction has most widely been treated within Eshelby-based modeling framework (Mura, 2012), as the so-called *inclusion* problem. From a physical standpoint, the current simulations provide an important physical foundation to understand the *inclusion*-type effects (i.e. generation of local fields under zero farfield stress) from the underlying atomistics.

Micromechanically, the origin of the interfacial elastic fields in an otherwise stress-free crystal is modeled via imposing the so-called eigenstrain. In our model, the  $\text{Ni}_4\text{Ti}_3$  precipitate is pre-constructed as the Ni-rich rhombohedral lattice of the lens-shaped geometry. On insertion into the B2 lattice, the lenticular-shaped precipitate creates a coherent periphery with the austenitic matrix, free of any interface dislocation. However, the local atomic coordination, adjacent both to the B2 matrix and the rhombohedral precipitate, differs significantly. The natural tendency of the atoms at the boundary would be to occupy the space in the most energetically favorable positions, thus minimizing the strong inter-lattice disregistry. Following the energy minimization in molecular statics simulations, the peripheral atoms assume metastable and higher potential energy states compared to those in the surrounding crystal. As a result, these atoms create long-range elastic disturbances, which reach the maximum magnitude very close to the interface (several nanometers), and subside spatially away from the precipitate. Thus, the genesis of the interfacial stress fields can be ascribed to the elastic stretching of atomic bonds at the boundary due to local atomic re-arrangement upon the energy minimization. The current predictions of the stress distributions are especially unique, in that these fields are generated as a direct outcome of underlying atomistic interactions, unlike the micro-mechanical approach (where separate mathematical terms are incorporated in the strain formulations to account for the existent disturbance). Moreover, in micromechanical approaches, the constancy of stiffness (both of the precipitate and the matrix) and a perfect lenticular shape are assumed, which is generally not the case in nature. From a physical standpoint, the molecular statics crystal configurations are closest to the real material ones. As a result, the currently computed stress gradient is in good agreement with the experimental ones as measured by Tirry and Schryvers (2005).

The lenticular geometry of the precipitates plays a crucial role in generating non-symmetric stress fields. Early quantum mechanical calculations demonstrated Wagner and Windl (2009) that the largest difference in elastic moduli between the cubic and rhombohedral lattices exists along the  $\langle 111 \rangle_{\text{R}} \parallel \langle 111 \rangle_{\text{B}_2}$ . As a result, the precipitates are always formed as oblate spheroids with disc-plane parallel to  $\{111\}_{\text{B}_2}$  family of planes. Due to the same rationale, a lens-shaped precipitate imposes direction-dependent stress fields. As a result of the directional nature of elastic fields, the stress concentrations near the surface experience a peak magnitude (as predicted by the our simulations as well as measured through experiments (Tirry and Schryvers, 2005)) The current results, in conjunction with the experimental ones, serve to establish the strongly directional nature of the precipitate fields. This result also bears important implications regarding the experimentally observed multiple variants of the precipitates discussed as follows.

It is known that there exist 4 types of precipitate variants lying of the  $\{111\}_{\text{B}_2}$  family of planes. The fields associated with each variant would be essentially identical in nature, and differ in orientation only. Thus, in order to isolate the nature/role of individual precipitates, it suffices to investigate only one variant case. It can be reasonably inferred that the presence of multiple precipitates would lead to a complex network of interacting fields in real materials. The mechanistic influences that these localized stresses would have on the phase transformation preferences would be fundamentally similar to the current observations, varying only in intensity and directionality.

### 4.2. Phase transformation and constitutive behavior

#### Transformation crystallography

The observed difference in the constitutive responses between the un-precipitated and the precipitated NiTi crystals (Fig. 9) is principally a result of: (a) the uni-directionality of the phase transformation and (b) how the coherent  $\text{Ni}_4\text{Ti}_3$  precipitate fields affect the phase transformation preferences (Bataillard et al., 1998). As observed, the B2  $\rightarrow$  B19' phase transformation is associated with the process of compound twinning on the  $\{111\}_{\text{B}_2}$  family of planes. The local fields would essentially result in a large resolved shear stress (RSS) on some variants and a small RSS for others based on: (i) the loading direction (i.e. tension or compression), (ii) crystallographic orientation of the austenite single crystal, and (iii) the orientation of the precipitate. Therefore, for a particular combination of these factors, different sets of transformation systems would be more readily available for activation. As a result, the presence of the precipitate would ultimately dictate the favored activation of certain variant systems (out of 24 possible ones as per the transformation crystallography). For the current case, we have considered only one combination of the precipitate variant and applied loading direction/

orientation. Further investigation of different loading type (i.e. tension) and crystal orientation remains a promising future research. We rationalize the currently observed trends in the levels of  $\sigma_{\text{transform}}$  and  $\epsilon_{\text{transform}}$  with regard to the crystallography as dictated by the local fields.

#### Transformation stress, $\sigma_{\text{transform}}$

The predicted  $\sigma_{\text{transform}}$  level is found to be reduced due to the presence of the precipitate fields (Fig. 9 and Table 1), in general agreement with the experimental trends in the literature (Gall et al., 1999; Sehitoglu et al., 2001). This behavior is believed to be an outcome of the local stress fields reinforcing the applied RSS. Thus, a lesser degree of externally applied loads would be required to initiate and sustain the progression of phase transformation on the locally favored variant systems. As a result, the  $\sigma_{\text{transform}}$  as well as the overall hardening response is decreased. Also noteworthy is the fact that flow behavior over the plateau for the precipitated crystal does not undergo any softening (as is the case for the un-precipitated one). The reason is believed to be attributable to the interaction among the variants (Fig. 11) giving rise to a hardening effect.

The current observations bear important mechanistic implications in interpreting the experimental behaviors. In real materials, the precipitates, being dispersed on 4 different  $\{111\}_{\text{B2}}$  planes, form a closely-knitted network of interacting stress fields. Since there exist 24 different sets of potential variants, some variants would always be locally triggered by a favorable field. By studying one isolated precipitate case, one can extend the current inferences towards elucidating the presence of multi-particles. Earlier literature noted that the precipitate-induced phase transformation is often accompanied by a transient R phase (of orthorhombic lattice type). However, Nishida and Wayman (1988) provided evidence that the R-phase is not an essential precursor to martensitic (B19') transformation. Additionally, Treppmann and Hornbogen (1995) noted that R-phase transformation occurs only when the precipitates are widely dispersed with interspersed stress fields, which is not the current case. In the present model, the B2 lattice directly converts into the B19' type martensitic lattice in the form of different martensitic variants (via compound twinning).

#### Transformation strain, $\epsilon_{\text{transform}}$

As the martensitic variants grow, the interfacial misfit would be modified, and so would be the extent of the local fields. Once the B2  $\rightarrow$  B19' transformation is complete, a new form of local mismatch would arise at the boundary between the rhombohedral precipitate and the B19' martensite. The newly generated stress fields now governs the reverse B19'  $\rightarrow$  B2 transformation during unloading, and hence the transformation strain,  $\epsilon_{\text{transform}}$ . Upon unloading, the maximum recoverable strain i.e. the  $\epsilon_{\text{transform}}$  for the precipitated crystal is lower than the recoverable strain of the un-precipitated crystal (3.18% versus 4.20% respectively as in Table 1). This behavior has also been noted in the earlier experimental literature. The currently observed  $\epsilon_{\text{transform}}$  reduction can be attributed to the combined effects of: (a) the non-transformability of the  $\text{Ni}_4\text{Ti}_3$  rhombohedral lattice, (b) the reverse transformation under the influence of a modified local stress concentration as mentioned earlier, and (c) the inhibition of de-twinning of martensite due to the precipitate, thus promoting easily recoverable elastic straining of martensite during loading (Treppmann et al., 1995).

#### Temperature effects

In addition, increasing temperature (300 K  $\rightarrow$  340 K) is observed to reduce the  $\epsilon_{\text{transform}}$  as well as increase the  $\sigma_{\text{transform}}$  levels (Table 1) both for the precipitated and the un-precipitated alloys. These observations from the simulations are in general agreement with literature experimental findings (Otsuka and Ren, 2005). The temperature effects can be rationalized on the basis of the thermodynamics of transforming alloys (Boyd and Lagoudas, 1996). The twinned monoclinic B19' structure constituting the martensite phase becomes unstable at elevated temperatures. In order to sustain the B2-to-B19' transformation, additional mechanical driving force is needed to be applied. As a result, the  $\sigma_{\text{transform}}$  levels continue to increase with rising temperature, quite unlike any conventional alloys (which would undergo decreasing flow stress). Simulation-wise, a gradually decreasing presence of the twinned B19' crystal has been noticed on analyzing the atomistic snapshots. At sufficiently high temperature, the parent B2 austenite behaves like a common alloy (i.e. demonstrates temperature-dependent plastic deformation of the austenite phase), no longer displaying any reversible transformation or the superelastic deformation.

#### Strain rate effects

Furthermore, it is important to note that the typical MD simulations are performed over several picoseconds timeframe. As a result, the deformation proceeds with a rather high strain-rate. However, the currently predicted constitutive responses are quite intriguingly in a reasonable agreement with the earlier experimental levels (conducted at a typical laboratory rate) (Orgéas and Favier, 1998; Sehitoglu et al., 2001). Experimentally, very high strain-rate deformation of NiTi austenite is associated with an increased hysteresis and the loss of pseudoelasticity due principally to: (a) the slipping of austenite crystal (Nemat-Nasser et al., 2005) and/or (b) the adiabatic heat generation (Leo et al., 1993). However, none of

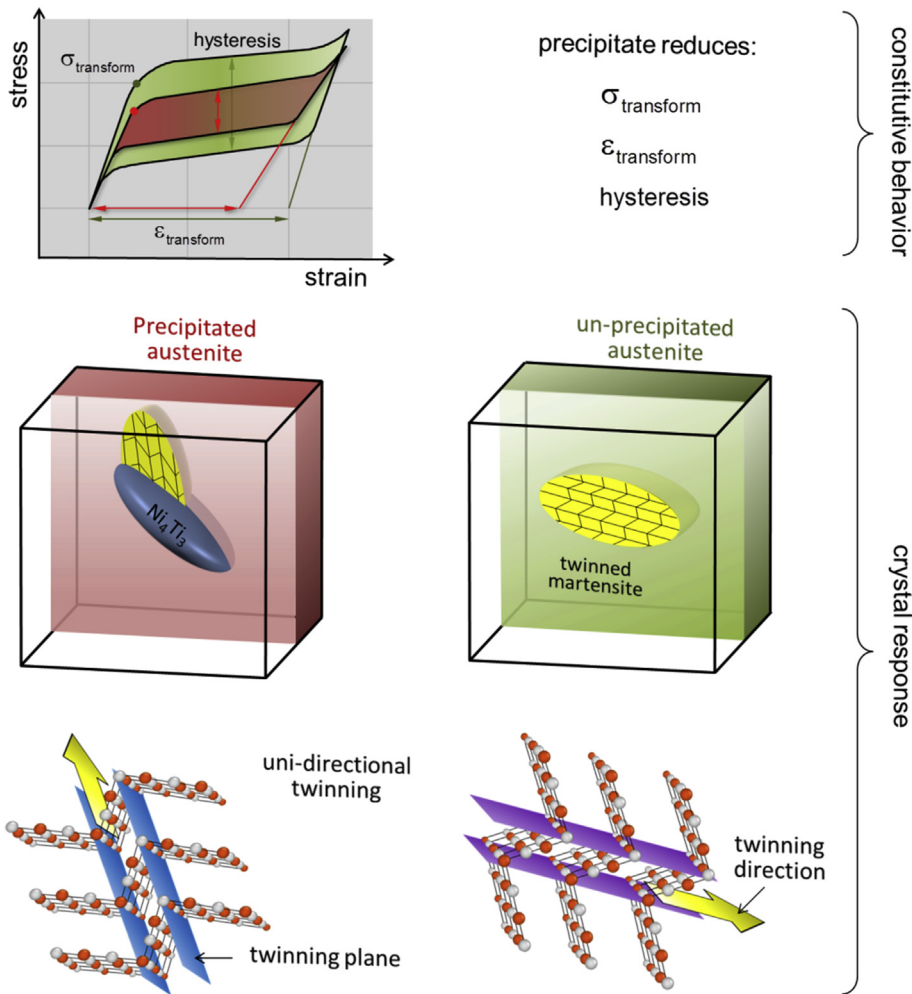


Fig. 12. Schematic summary of the findings from the current modeling.

these phenomena is present in the current molecular dynamics deformations, which proceeds solely via compound twinning. Early literature reports that pure twinning is considerably rate-insensitive unlike dislocation slip (Meyers et al., 2001). In addition, the heat flow rate during the current simulations was kept in synchronization with the strain rates, thereby producing no adiabatic entrapment of deformation-generated heat. As a result, the simulated deformation scenario is mechanistically very similar to the experimental deformation at the laboratory settings. Due to the foregoing factors, the present levels of the stress–strain curves are not affected by the usually encountered high rate-related artifacts in the MD modeling (as cross-validated by performing multiple simulations at different strain rates).

## 5. Summary and future

In the current paper, we have predicted the internal/external stress distribution surrounding a coherent  $\text{Ni}_4\text{Ti}_3$  precipitate (with a disc diameter of 7 nm). The local fields are generated as a direct outcome of the inter-lattice mismatch between the cubic B2 matrix and the rhombohedral  $\text{Ni}_4\text{Ti}_3$  precipitate. Hence, the origin of the precipitate stress fields is captured on a physical ground. Next, the constitutive behaviors of the precipitated austenite are studied against the un-precipitated pristine crystal under the  $\langle 011 \rangle_{\text{B2}}$  compression. The information obtained from the current model is schematically illustrated in Fig. 12. A reduced degree of the transformation stress, strain and hysteresis is observed to have resulted for the precipitated alloy. The atomistic origins of the overall constitutive behaviors have been correlated with: (a) the unidirectionality of the phase transformation (i.e. internal twinning of B19' lattice), (b) the local stress fields setting preference for the activation of different variant systems, and (c) the thermodynamics of the transformation alloys. In addition, the principal merit of the current modeling endeavor is highlighted as clarifying the atomic-scale roles of a coherent precipitate in improving the NiTi superelastic traits. The successful modeling of the precipitate problem implies important future extension.

The feasibility of the current atomistic simulations also suggests considerable promise for future research. For example, problems such as fracture and fatigue behaviors of SMAs remain major issues today to be addressed. Atomistic simulations can most effectively be employed to probe into the cracking phenomena under static and/or cyclic loading conditions. The poor fatigue and fracture performances are at present a major setback for further extending the NiTi SMA usage (Robertson et al., 2012) as demonstrated experimentally. Thus, utilizing atomistics, mesoscale defect properties such as Peierls stresses could be predicted (Alkan et al., 2016; Chowdhury et al., in press), which in turn could be used in continuum damage evaluation (Chowdhury et al., 2014b; Hazar et al., 2015). Such knowledge would be helpful for designing better SMAs in the future.

## Acknowledgment

This research was supported by the Nyquist chair funds. We acknowledge the use of the parallel computing resource, the Taub cluster, at the University of Illinois.

## References

- Alkan, S., Chowdhury, P., Sehitoğlu, H., Rateick, R.G., Maier, H.J., 2016. Role of nanotwins on fatigue crack growth resistance—Experiments and theory. *Int. J. Fatigue* 84, 28–39.
- Bataillard, L., Bidaux, J.-E., Gotthardt, R., 1998. Interaction between microstructure and multiple-step transformation in binary NiTi alloys using in-situ transmission electron microscopy observations. *Philos. Mag. A* 78, 327–344.
- Bhattacharya, K., 2003. *Microstructure of Martensite: Why it Forms and How it Gives Rise to the Shape-memory Effect*. Oxford University Press.
- Bouvet, C., Calloch, S., Lexcelle, C., 2004. A phenomenological model for pseudoelasticity of shape memory alloys under multiaxial proportional and nonproportional loadings. *Eur. J. Mech. A/Solids* 23, 37–61.
- Boyd, J.G., Lagoudas, D.C., 1996. A thermodynamical constitutive model for shape memory materials. Part I. The monolithic shape memory alloy. *Int. J. Plast.* 12, 805–842.
- Buehler, W.J., Gilfrich, J.V., Wiley, R.C., 1963. Effect of low-temperature phase changes on the mechanical properties of alloys near composition TiNi. *J. Appl. Phys.* 34, 1475–1477.
- Chang, L.C., Read, T.A., 1951. The gold-cadmium beta phase. *Trans. AIME* 191, 47.
- Chowdhury, P., 2011. *Fatigue Crack Growth (FCG) Modeling in the Presence of Nano-obstacles*. University of Illinois at Urbana-Champaign.
- Chowdhury, P., Ren, G., Sehitoğlu, H., 2015a. NiTi superelasticity via atomistic simulations. *Philos. Mag. Lett.* 95 (12), 574–586.
- Chowdhury, P., Sehitoğlu, H., Abuzaid, W., Maier, H., 2015b. Mechanical response of low stacking fault energy Co–Ni alloys—Continuum, mesoscopic and atomic level treatments. *Int. J. Plast.* 71, 32–61.
- Chowdhury, P., Sehitoğlu, H., Maier, H., Rateick, R., 2015c. Strength prediction in NiCo alloys—The role of composition and nanotwins. *Int. J. Plast.* (in press).
- Chowdhury, P.B., Sehitoğlu, H., Rateick, R.G., 2014a. Predicting fatigue resistance of nano-twinned materials: part I—role of cyclic slip irreversibility and Peierls stress. *Int. J. Fatigue* 68, 277–291.
- Chowdhury, P.B., Sehitoğlu, H., Rateick, R.G., 2014b. Predicting fatigue resistance of nano-twinned materials: part II—effective threshold stress intensity factor range. *Int. J. Fatigue* 68, 292–301.
- Chowdhury, P.B., Sehitoğlu, H., Rateick, R.G., Maier, H.J., 2013. Modeling fatigue crack growth resistance of nanocrystalline alloys. *Acta Mater.* 61, 2531–2547.
- Chumlyakov, Y.I., Kireeva, I., Panchenko, E.Y., Timofeeva, E.E., Kretinina, I., Kuts, O., Karaman, I., Maier, H., 2014. Shape memory effect and superelasticity in single crystals of high-strength ferromagnetic alloys. *Adv. Mater. Res.* 15–22. *Trans Tech Publ.*
- Chumlyakov, Y.I., Kireeva, I.V., Lineyev, V.N., Lwisyuk, A.G., 1997. Aging influence on the shape memory effects and superelasticity in titanium–nickel single crystals. In: *Proceedings of the 1996 MRS Fall Symposium, December 2, 1996–December 5, 1996*. Materials Research Society, Boston, MA, USA, pp. 387–392.
- Cisse, C., Zaki, W., Zineb, T.B., 2016. A review of constitutive models and modeling techniques for shape memory alloys. *Int. J. Plast.* 76, 244–284.
- Farkas, D., Roqueta, D., Vilette, A., Ternes, K., 1996. Atomistic simulations in ternary Ni–Ti–Al alloys. *Model. Simul. Mater. Sci. Eng.* 4, 359.
- Frenkel, D., Smit, B., 2001. *Understanding Molecular Simulation: from Algorithms to Applications*. Academic press.
- Gall, K., Sehitoğlu, H., Chumlyakov, Y.I., Kireeva, I.V., Maier, H.J., 1999. The influence of aging on critical transformation stress levels and martensite start temperatures in NiTi: part II—discussion of experimental results. *J. Eng. Mater. Technol.* 121, 28–37.
- Giannozzi, P., Baroni, S., Bonini, N., Calandra, M., Car, R., Cavazzoni, C., Ceresoli, D., Chiarotti, G.L., Cococcioni, M., Dabo, I., 2009. Quantum Espresso: a modular and open-source software project for quantum simulations of materials. *J. Phys. Condens. Matter* 21, 395502.
- Hazar, S., Zaki, W., Moumni, Z., Anlas, G., 2015. Modeling of steady-state crack growth in shape memory alloys using a stationary method. *Int. J. Plast.* 67, 26–38.
- Johnson, A.W., Sehitoğlu, H., Hamilton, R., Biallas, G., Maier, H., Chumlyakov, Y., Woo, H., 2005. Analysis of multistep transformations in single-crystal NiTi. *Metall. Mater. Trans. A* 36, 919–928.
- Khalil-Allafi, J., Dlouhy, A., Eggeler, G., 2002. Ni<sub>4</sub>Ti<sub>3</sub>-precipitation during aging of NiTi shape memory alloys and its influence on martensitic phase transformations. *Acta Mater.* 50, 4255–4274.
- Kudoh, Y., Tokonami, M., Miyazaki, S., Otsuka, K., 1985. Crystal structure of the martensite in Ti-49.2 at.% Ni alloy analyzed by the single crystal X-ray diffraction method. *Acta Metall.* 33, 2049–2056.
- Lai, W., Liu, B., 2000. Lattice stability of some Ni–Ti alloy phases versus their chemical composition and disordering. *J. Phys. Condens. Matter* 12, L53.
- Leo, P.H., Shield, T., Bruno, O.P., 1993. Transient heat transfer effects on the pseudoelastic behavior of shape-memory wires. *Acta Metall. Mater.* 41, 2477–2485.
- Li, D., Chen, L., 1997. Shape of a rhombohedral coherent Ti<sub>11</sub>Ni<sub>14</sub> precipitate in a cubic matrix and its growth and dissolution during constrained aging. *Acta Mater.* 45, 2435–2442.
- Ma, J., Hornbuckle, B., Karaman, I., Thompson, G., Luo, Z., Chumlyakov, Y., 2013. The effect of nanoprecipitates on the superelastic properties of FeNiCoAlTi shape memory alloy single crystals. *Acta Mater.* 61, 3445–3455.
- Mercier, O., Melton, K., Gremaud, G., Hägi, J., 1980. Single-crystal elastic constants of the equiatomic NiTi alloy near the martensitic transformation. *J. Appl. Phys.* 51, 1833–1834.
- Meyers, M., Vöhringer, O., Lubarda, V., 2001. The onset of twinning in metals: a constitutive description. *Acta Mater.* 49, 4025–4039.
- Mirzaeifar, R., Gall, K., Zhu, T., Yavari, A., DesRoches, R., 2014. Structural transformations in NiTi shape memory alloy nanowires. *J. Appl. Phys.* 115, 194307.
- Mishin, Y., 2004. Atomistic modeling of the  $\gamma$  and  $\gamma'$ -phases of the Ni–Al system. *Acta Mater.* 52, 1451–1467.
- Miyazaki, S., Kimura, S., Otsuka, K., Suzuki, Y., 1984. The habit plane and transformation strains associated with the martensitic transformation in Ti–Ni single crystals. *Scr. Metall.* 18, 883–888.
- Mura, T., 2012. *Micromechanics of defects in solids*. Springer Science & Business Media.
- Mutter, D., Nielaba, P., 2010. Simulation of structural phase transitions in NiTi. *Phys. Rev. B* 82, 224201.
- Mutter, D., Nielaba, P., 2011. Simulation of the thermally induced austenitic phase transition in NiTi nanoparticles. *Eur. Phys. J. B* 84, 109–113.

- Mutter, D., Nielaba, P., 2013. Simulation of the shape memory effect in a NiTi nano model system. *J. Alloys Compd.* 577, S83–S87.
- Nemat-Nasser, S., Choi, J.-Y., Guo, W.-G., Isaacs, J.B., 2005. Very high strain-rate response of a NiTi shape-memory alloy. *Mech. Mater.* 37, 287–298.
- Nishida, M., Wayman, C., 1988. Electron microscopy studies of the “Premartensitic” transformations in an aged Ti-51 at% Ni shape memory alloy. *Metallography* 21, 255–273.
- Orgéas, L., Favier, D., 1998. Stress-induced martensitic transformation of a NiTi alloy in isothermal shear, tension and compression. *Acta Mater.* 46, 5579–5591.
- Otsuka, K., Ren, X., 2005. Physical metallurgy of Ti–Ni-based shape memory alloys. *Prog. Mater. Sci.* 50, 511–678.
- Patoo, E., Eberhardt, A., Berveiller, M., 1996. Micromechanical modelling of superelasticity in shape memory alloys. *Le J. Phys. IV* 6, C1–277–C271–292.
- Plimpton, S., 1995. Fast parallel algorithms for short-range molecular dynamics. *J. Comput. Phys.* 117, 1–19.
- Robertson, S., Pelton, A., Ritchie, R., 2012. Mechanical fatigue and fracture of Nitinol. *Int. Mater. Rev.* 57, 1–37.
- Saburi, T., Nenno, S., Fukuda, T., 1986. Crystal structure and morphology of the metastable X phase in shape memory Ti-Ni alloys. *J. Less Common Metals* 125, 157–166.
- Schetky, L.M., 1979. Shape memory alloys, Nov. 1979. *Sci. Am.* 241, 74–82.
- Schryvers, D., Tirry, W., Yang, Z., 2006. Measuring strain fields and concentration gradients around Ni<sub>4</sub>Ti<sub>3</sub> precipitates. *Mater. Sci. Eng. A* 438, 485–488.
- Sedláč, P., Frost, M., Benešová, B., Zineb, T.B., Šittner, P., 2012. Thermomechanical model for NiTi-based shape memory alloys including R-phase and material anisotropy under multi-axial loadings. *Int. J. Plast.* 39, 132–151.
- Sehitoglu, H., Jun, J., Zhang, X., Karaman, I., Chumlyakov, Y., Maier, H., Gall, K., 2001. Shape memory and pseudoelastic behavior of 51.5% Ni–Ti single crystals in solutionized and overaged state. *Acta Mater.* 49, 3609–3620.
- Sehitoglu, H., Karaman, I., Anderson, R., Zhang, X., Gall, K., Maier, H., Chumlyakov, Y., 2000. Compressive response of NiTi single crystals. *Acta Mater.* 48, 3311–3326.
- Sehitoglu, H., Zhang, X., Kotil, T., Canadinc, D., Chumlyakov, Y., Maier, H., 2002. Shape memory behavior of FeNiCoTi single and polycrystals. *Metall. Mater. Trans. A* 33, 3661–3672.
- Shaw, J.A., 2000. Simulations of localized thermo-mechanical behavior in a NiTi shape memory alloy. *Int. J. Plast.* 16, 541–562.
- Song, Z., Dai, H.-H., Sun, Q.-P., 2013. Propagation stresses in phase transitions of an SMA wire: new analytical formulas based on an internal-variable model. *Int. J. Plast.* 42, 101–119.
- Stukowski, A., 2010. Visualization and analysis of atomistic simulation data with OVITO—the open visualization tool. *Model. Simul. Mater. Sci. Eng.* 18, 015012.
- Tadaki, T., Nakata, Y., Shimizu, K.i., Otsuka, K., 1986. Crystal structure, composition and morphology of a precipitate in an aged Ti-51 at% Ni shape memory alloy. *Trans. Jpn. Inst. Metals* 27, 731–740.
- Tadmor, E.B., Miller, R.E., 2011. *Modeling Materials: Continuum, Atomistic and Multiscale Techniques*. Cambridge University Press.
- Tanaka, Y., Himuro, Y., Kainuma, R., Sutou, Y., Omori, T., Ishida, K., 2010. Ferrous polycrystalline shape-memory alloy showing huge superelasticity. *Science* 327, 1488–1490.
- Tirry, W., Schryvers, D., 2005. Quantitative determination of strain fields around Ni<sub>4</sub>Ti<sub>3</sub> precipitates in NiTi. *Acta Mater.* 53, 1041–1049.
- Treppmann, D., Hornbogen, E., 1995. The effect of dislocation substructure and decomposition on the course of diffusionless transformations. *Le J. Phys. IV* 5, C2–211–C212–216.
- Treppmann, D., Hornbogen, E., Wurzel, D., 1995. The effect of combined recrystallization and precipitation processes on the functional and structural properties in NiTi alloys. *J. Phys IV* 5, C8–569–C568–574.
- Wagner, M.F.-X., Windl, W., 2009. Elastic anisotropy of Ni<sub>4</sub>Ti<sub>3</sub> from first principles. *Scr. Mater.* 60, 207–210.
- Wang, J., Sehitoglu, H., 2014. Martensite modulus dilemma in monoclinic NiTi-theory and experiments. *Int. J. Plast.* 61, 17–31.
- Wang, X., Kustov, S., Verlinden, B., Van Humbeeck, J., 2015. Fundamental development on utilizing the R-phase transformation in NiTi shape memory alloys. *Shape Mem. Superelast.* 1–9.
- Yamauchi, K., Ohkata, I., Tsuchiya, K., Miyazaki, S., 2011. *Shape Memory and Superelastic Alloys: Applications and Technologies*. Elsevier.
- Yang, Q., Li, G., 2015. Temperature and rate dependent thermomechanical modeling of shape memory polymers with physics based phase evolution law. *Int. J. Plast.* (in press).
- Zaki, W., Moumni, Z., 2007. A three-dimensional model of the thermomechanical behavior of shape memory alloys. *J. Mech. Phys. Solids* 55, 2455–2490.
- Zhong, Y., Gall, K., Zhu, T., 2012. Atomistic characterization of pseudoelasticity and shape memory in NiTi nanopillars. *Acta Mater.* 60, 6301–6311.
- Zope, R.R., Mishin, Y., 2003. Interatomic potentials for atomistic simulations of the Ti–Al system. *Phys. Rev. B* 68, 024102.